Top Catal (2013) 56:623–629
DOI 10.1007/s11244-013-0022-5

ORIGINAL PAPER

Hydrothermal Synthesis of Mesoporous Bi_2O_3/Co_3O_4 Microsphere and Photocatalytic Degradation of Orange II Dyes by Visible Light

Shu-Han Hsieh · Gang-Juan Lee · Chin-Yi Chen · Jing-Heng Chen · Shih-Hsin Ma · Tzyy-Leng Horng · Kun-Huang Chen · Jerry J. Wu

Published online: 12 April 2013

Abstract New visible-light-responsive porous Bi_2O_3/Co_3O_4 microspheres have been successfully synthesized by hydrothermal method in ethylene glycol (EG) accompanied with the addition of polyethyleneglycol (PEG) and sodium acetate. PEG can enter into the initial nuclei because of the similar structure and composition with EG, resulting in the formation of hollow porous structures. The specific surface area incorporating bismuth and cobalt oxides is enlarged by comparing with their pristine forms. According to the photocatalysis results, Bi_2O_3/Co_3O_4 composite microsphere is more effective to degrade Orange II dye than pure Bi_2O_3 photocatalyst by better utilizing visible light activities.

Keywords Photocatalyst · Microsphere · Bi_2O_3/Co_3O_4 · Orange II

S.-H. Hsieh · G.-J. Lee · J. J. Wu (✉)
Department of Environmental Engineering and Science, Feng Chia University, Taichung 407, Taiwan
e-mail: jjwu@fcu.edu.tw

C.-Y. Chen
Department of Material Engineering and Science, Feng Chia University, Taichung 407, Taiwan

J.-H. Chen · S.-H. Ma
Department of Photonics, Feng Chia University, Taichung 407, Taiwan

T.-L. Horng
Department of Applied Mathematics, Feng Chia University, Taichung 407, Taiwan

K.-H. Chen
Department of Electric Engineering, Feng Chia University, Taichung 407, Taiwan

1 Introduction

The fabrication of highly efficient and visible light responsive photocatalyst is a key topic among photocatalysis researches. Recently, much attention has been paid to the preparation of photocatalyst with morphological and surface-structured control [1, 2]. Functional materials with new properties at low cost are important to applications in various fields. Since porous materials possess numbers of pores and active sites, they will substantially benefit photocatalytic reactions towards environmental contaminants. Larger pores of porous materials can promote rapid reactants transport through the porous catalysts, while smaller pores of porous materials provide high surface areas for reactant adsorption/desorption and more reaction sites for catalytic process [3]. The hollow materials have potential applications across different technological fields, owing to their well-defined interior voids, large specific surface area, and surface permeability. Hollow porous materials have been demonstrated to offer an adjustable environment for encapsulating the target pollutants on the internal surface of the pores which may increase the degradation rate substantially [4]. On the other hand, the light absorption property of the photocatalyst plays an important role in its photocatalytic efficiency. Bismuth oxide (Bi_2O_3) is recently an attractive material due to its good electrical conductivity, thermal properties, and narrow band-gap (2.8 eV). Up to now, Bi_2O_3 has been prepared by different methods with various morphologies and properties, such nanorod, nanoparticle, microsphere, nanofiber [5–7]. Duan et al. [8] have fabricated a 3-D flowerlike Bi_2O_3 by a hydrothermal method and Tseng et al. [9] have also prepared hierarchical bismuth oxide architectures via a solution precipitation.

Composite materials provide a way to enhance the photocatalytic activity by increasing the charge separation

and extending the visible light absorption. Due to the special f and d electron orbital structure, the rare earth elements and their oxides may be doped in Bi_2O_3 to improve conversion efficiency [10]. As an important magnetic p-type semiconductor, cobalt oxide is of special interest due to its potential applications, including sensors, heterogeneous catalysts, electrochromical devices, and magnetic materials [11]. Co_3O_4 belongs to the normal spinel crystal structure based on a cubic close packing array of oxide ions, in which Co(II) ions occupy the tetrahedral 8a sites and Co(III) ions occupy the octahedral 16d sites [12]. Due to the significant effect of particle size and morphology on the properties of such materials, it is always the researchers' purpose to control the particles sizes and morphologies of Co_3O_4. The azo compound is one of the most important groups of dyes used in photocatalytic processes. Among the azo dyes, Orange II has been used as a model compound for the studies of oxidation degradation by different photocatalysts [13, 14]. Few literatures have focused on micro-and nano-scale composite Co_3O_4 hollow microspheres with high purity and homogeneous size.

The effect of various experimental parameters on the formation of Bi_2O_3/Co_3O_4 via hydrothermal processes was investigated in this study. The influence of applying polyethyleneglycol (PEG) and sodium acetate on the morphology and surface properties of catalyst materials were also conducted. In this work, we focused on the synthesis of Co_3O_4, Bi_2O_3, and Bi_2O_3/Co_3O_4 composite particles by hydrothermal process and their photocatalytic activities under visible light illumination.

2 Materials and Methods

4 mol $Bi(NO_3)_3{\cdot}5H_2O$ (1.94 g) and 2 mol $Co(NO_3)_3{\cdot}6H_2O$ (0.291 g) were dissolved in a mixed solution that contained ethylene glycol (EG) (35 mL), PEG (1.4 g), and sodium acetate (CH_3COONa, NaAc) (3 g). The mixed solution was stirred and gradually became transparent, then sealed in a Teflon-lined stainless-steel autoclave (200 mL capacity). The autoclave was heated and maintained at 180 °C for 12 h, and allowed to cool down at room temperature followed by vigorous stirring for an hour. The product was washed with deionized water and ethanol several times, and dried in a vacuum condition. Finally, the cayalyst was calcined at 500 °C for 2 h to obtain crystalline bismuth/cobalt oxide composites. The pristine Co_3O_4 and Bi_2O_3 were also prepared via the same synthetic procedures, respectively.

A 200 mL capacity borosilicate glass photoreactor was used in all experiments. The photocatalytic degradation of Orange II was conducted at neutral pH (pH 7.0) and 25 °C, controlled by a circulating bath. The dosing amount of the as-synthesized catalyst (0.2 g) and Orange II (10 mg/L) were used the same for all experiments. In order to ensure adsorption/desorption equilibrium, the solution was stirred for about 30 min in dark prior to the initiation of the experiments. A xenon lamp (350 W) was used as a visible light source with a cutoff filter ($\lambda \geqq 400$ nm). About 5 mL of the solution was withdrawn at given irradiation time intervals to determine the degradation percentage of dye with time. At the apparent disappearance of the substrate, Orange II absorbance was determined using UV–Vis spectrophotometer (Shimadzu Instruments, Japan) at the wavelength of 485 nm. Prior to the analysis, the catalyst was removed from samples by centrifugation and filtration using a 0.22 μm polyvinylidene fluoride filter.

The X-ray diffraction (XRD) patterns were recorded using an X'Pert PRO PAN analytical diffractometer with a scanned angle 2θ from 10° to 100°. The morphology was examined by a JSM6700F field-scanning electron microscope (FE-SEM). Specific surface areas and pore size/volume distribution were computed from the results of N_2 physisorption at 77 K (Micromeritics ASAP 2020) by the analysis of BET (Brunauer–Emmet–Teller) and BJH (Barrett–Joyner–Halenda). The degassing temperature of BET measurement was 120 °C. The X-ray photoelectron spectra were collected on an ESCA X-ray photoelectron spectrometer (XPS), using a Mg Kα X-ray as the excitation source.

3 Results and Discussion

The formation of Bi_2O_3/Co_3O_4, Bi_2O_3, and Co_3O_4 was confirmed by the XRD spectrum. Furthermore, the crystal structure of Bi_2O_3/Co_3O_4 nanoparticles was determined from the powder XRD patterns. The XRD patterns (Fig. 1) have indicated that Bi_2O_3/Co_3O_4 nanoparticles are different while compared to that of pristine Co_3O_4 (JCPDS No.74–1656) and Bi_2O_3 (JCPDS No. 71–2274) nanoparticles. The diffraction peak of Bi_2O_3 is good agreement with standard value, which can be seen at $2\theta = 27.393$ (JCPDS card No. 71–2274), belonging to (121) phase and a monoclinic system with $a = 5.848$ Å, $b = 8.166$ Å, and $c = 7.509$ Å. The diffraction peak of Co_3O_4 is shown at $2\theta = 36.936$ (JCPDS card No. 74–1656), belonging to (311) phase and a cubic system with $a = 8.065$ Å. In addition, no peaks of other impurities were observed in the XRD pattern.

The morphologies of Bi_2O_3/Co_3O_4 were affected during the material fabrication by adding different amounts of sodium acetate and changing reaction time. In our study, we have synthesized Bi_2O_3/Co_3O_4 microsphere by the hydrothermal method incorporating with sodium acetate.

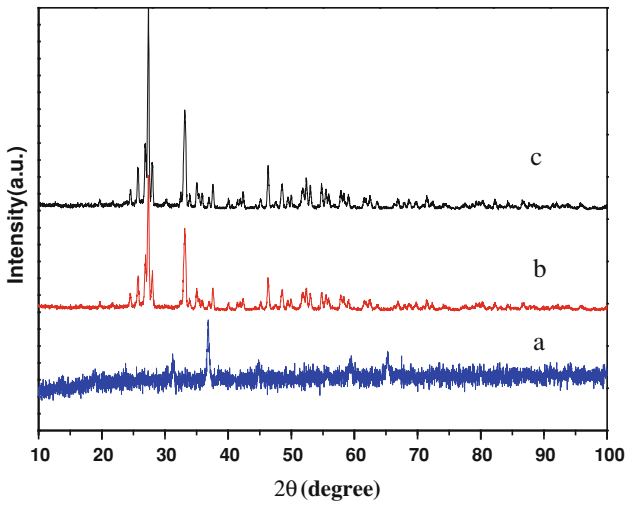

Fig. 1 XRD spectra of (*a*) Co_3O_4, (*b*) Bi2O3/Co_3O_4, and (*c*) Bi_2O_3

The structural morphologies of Bi_2O_3/Co_3O_4 catalyst prepared by hydrothermal method were observed by scanning electron microscope (Fig. 2). The SEM images (Fig. 2a–d) for Bi_2O_3/Co_3O_4 without and with the use of NaAc are somewhat different. Without the addition of NaAc, the morphology is more like flake structure. However, the morphology would become porous structures while adding NaAc template. The size of as-synthesized microspheres ranges approximately 2–6 μm. When increasing the NaAc concentration from 0.5 g to 2 g, it was found that the porous structure would become disappeared (Fig. 2e, f). The reason for such assembled structures may be due to the bridging of Co–O–Co or Co–O–O–Co units made up of edge-sharing CoO_n units arranged in planar arrays [15, 16]. EG in solution adsorbs Bi^{3+} and Co^{2+} to form a relatively stable complex, then Bi_2O_3/Co_3O_4 are obtained by means of the hydrolyzation of $Bi_2(OCH_2CH_2O)_3$ in solution. Finally, as the mass diffusion and Ostwald ripening process proceed, the nanosheets start to grow and be accompanied by their self-organization into the spherical structure on the surfaces. In addition, the FE-SEM in Fig. 3 clearly reveals that the concentration of NaAc strongly influenced the porous characteristics on the spherical surface of Bi_2O_3/Co_3O_4. Without NaAc addition, the morphologies of Bi_2O_3/Co_3O_4 present the flake structure with smooth surface. However with NaAc addition, the morphologies of Bi_2O_3/Co_3O_4 show porous microsphere. Since the formation of hollow microspheres is very sensitive to the concentration of NaAc, the lower and higher concentration will only form nanosheets rather than the hollow microspheres [17]. From the results, the EG can play an important role in the formation of porous morphologies. NaAc was selected for electrostatic stabilization, thus preventing particles agglomerating during the formation in the liquid phase process [18, 19]. Another important advantage of NaAc is to increase the alkalinity of reaction system after hydrolysis, which favors the reduction of $Co(NO_3)_3$ into Co_3O_4. In this condition provided by EG and NaAc at high temperature, Bi_2O_3/Co_3O_4 materials are finally formed through dehydration. The SEM images in Fig. 3 indicate that the formation of the hollow microsphere is dependent on the presence of PEG. Without PEG, only solid porous microspheres composed of nanosheets were obtained [17]. When PEG was applied, PEG might enter into the initial nuclei because of the similar structure and composition with EG. It is favorable for the dissolution of the inner part of solid microspheres, thus resulting in the formation of hollow microspheres composed of nanosheets in ripening process.

In the XPS analysis, no peaks of other elements, except C, O, Co, and Bi, were observed, indicating the high purity of the as-synthesized composite (Fig. 4a). In the XPS spectra of the as-prepared Bi_2O_3/Co_3O_4 catalyst, Bi ($4f_{7/2}$) and Bi ($4f_{5/2}$) peaks lie at 158.2 eV and 163.4 eV (Fig. 4d), the C (1s) peak lies at 284 eV, and Co ($2p_{1/2}$) and Co ($2p_{3/2}$) peaks lie at 794.8 and 779.8 eV (Fig. 4c). The Co_3O_4 spectrum contains smaller satellite features located about 9 eV, which is higher in binding energy than the main peaks (Co $2p_{3/2}$) [20]. The weak 2p satellite features for the spinels are found at 788.0 and 804.6 eV with reduced intensity. The cobalt 2p spectrum obtained from Bi_2O_3/Co_3O_4 is consistent with Co^{2+} cations (CoO) in tetrahedral sites and Co^{3+} (Co_2O_3) cations in octahedral sites within the O^{2-} sublattice. Compared with the intensive CoO satellites, lower binding energies are found at 785.5 and 802.1 eV. XPS O 1s spectra obtained from the surface are shown in Fig. 4b. XPS for the O 1 s displays the oxygen in Bi oxide, Co oxide, and OH species adsorbed onto the surface. The core levels are centered at 529.8 and 530.6 eV, which are assigned as the oxygen in Bi and Co oxides, The main oxygen peak due to lattice O^{2-} is set to 529.6 eV, previously found for CoO and Co_3O_4, since both CoO and Co_3O_4 have O 1s BEs at this value. The binding energy of 531.1 eV is comparable to that reported for surface hydroxyls, under-coordinated lattice oxygens (O^-), chemisorbed oxygen, and inaccuracies in the peak fitting due to the inability to reproduce the exact peak shape and/or secondary electron background [21].

Co_3O_4, Bi_2O_3, and Bi_2O_3/Co_3O_4 photocatalysts prepared via hydrothermal method have different surface properties as shown in Table 1. As can be seen in Table 1, Bi_2O_3/Co_3O_4 possesses the highest surface area (45.6 m^2/g) and a pore volume (0.16 cm^3/g), which is mainly due to its hollow structure. Although the surface area of Co_3O_4 is relatively low (12.3 m^2/g), the composite Bi_2O_3/Co_3O_4 shows better enhancement on surface area compared with pristine Bi_2O_3 (36.7 m^2/g). The enlarged BET is attributed to introducing the nanoparticles Co_3O_4 into the structure of Bi_2O_3. The N_2 adsorption and desorption isotherms for the

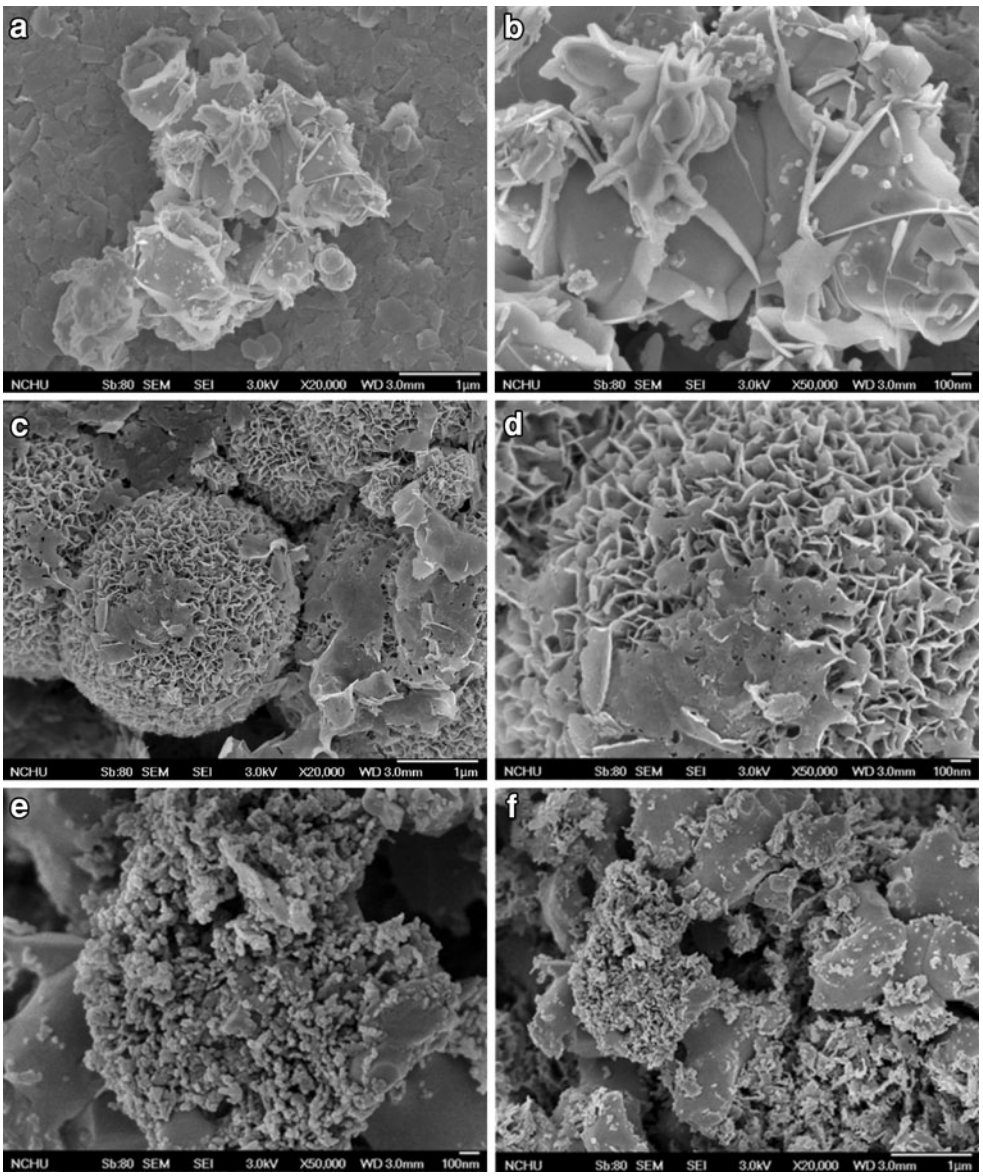

Fig. 2 FE-SEM images of Bi_2O_3/Co_3O_4 (without NaAc) (**a**, **b**), Bi_2O_3/Co_3O_4 (with 0.5 g of NaAc) (**c**, **d**), and Bi_2O_3/Co_3O_4 (with 2 g of NaAc) (**e**, **f**)

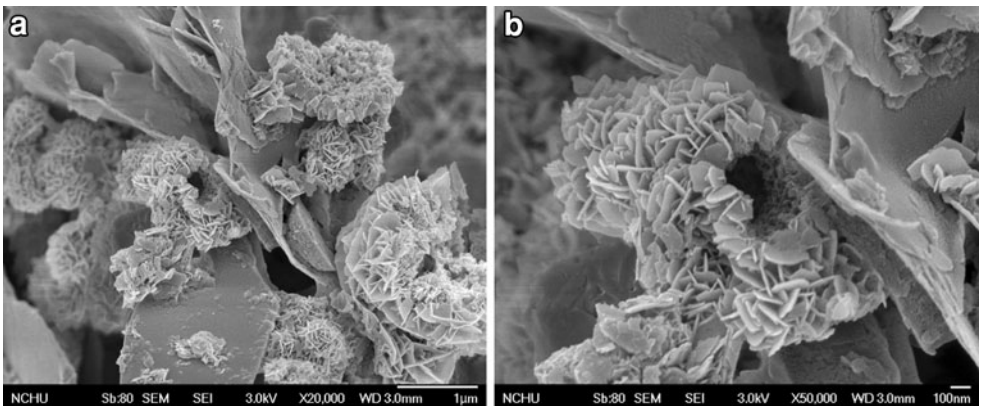

Fig. 3 FE-SEM images of Bi_2O_3/Co_3O_4 with hollow structure containing NaAc and PEG

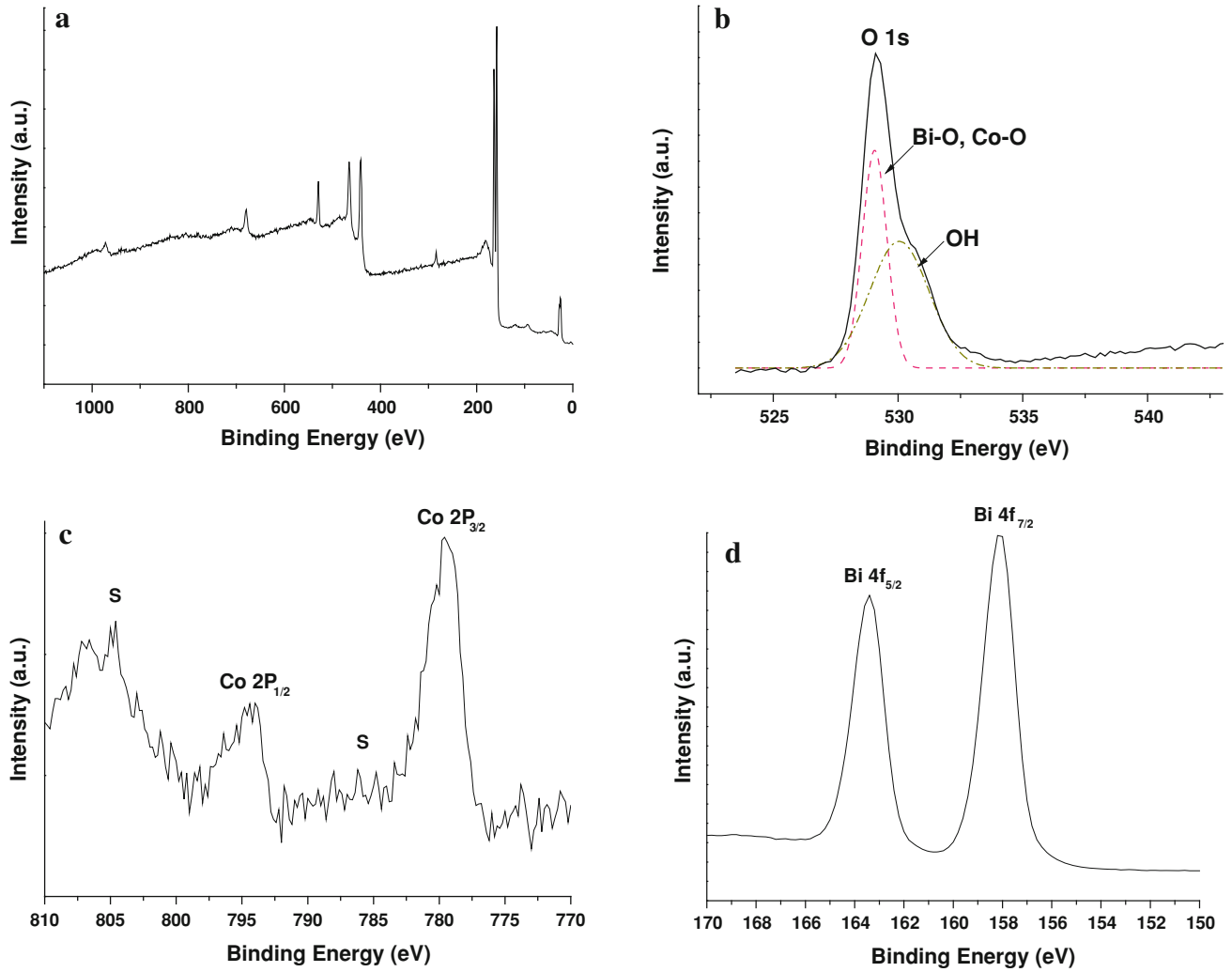

Fig. 4 **a** XPS full spectra of Bi_2O_3/Co_3O_4. **b** XPS spectra to show the presence of O ions in Bi_2O_3/Co_3O_4. **c** XPS spectrum to show the presence of Co ions in Bi_2O_3/Co_3O_4. **d** XPS spectra to show the presence of Bi ions in Bi_2O_3/Co_3O_4

Table 1 Surface properties of Bi_2O_3/Co_3O_4, Co_3O_4, and Bi_2O_3 photocatalysts

Hydrothermal method	BET surface area (m^2/g)	Pore size (Å)	Pore vol (cm^3/g)
Bi_2O_3/Co_3O_4	45.6	140.2	0.16
Co_3O_4	12.3	102	0.03
Bi_2O_3	36.7	88.7	0.08

Bi_2O_3/Co_3O_4 composite particle are provided in Fig. 5. It shows a typical type IV behavior with hysteresis loop characteristics of mesoporous materials.

We have also examined the photocatalytic activity of the synthesized Bi_2O_3/Co_3O_4 photocatalysts to degrade Orange II under visible light illumination ($\lambda \geq 400$ nm) as seen in Fig. 6. The Orange II dye concentration was only reduced 5.9 % after 5 h illumination by visible light in the absence of any photocatalyst, revealing that Orange II is difficult to be photodegraded by visible light directly. The comparison of the photocatalytic degradation of Orange II on all the catalysts studied was performed. The photocatalytic activity of Bi_2O_3/Co_3O_4 prepared by hydrothermal method showed that the Bi_2O_3/Co_3O_4 hybrid composites were more efficient than pristine Bi_2O_3 and Co_3O_4. A high Orange II removal efficiency was observed for Bi_2O_3/Co_3O_4 by removing 84.7 % of dye in 5 h compared to 65.8 and 48.9 % for Bi_2O_3 and Co_3O_4, respectively. Under visible light illumination, the pseudo-first-order rate constants (k) were calculated as 2.34×10^{-2} and 2.9×10^{-3} min^{-1}, respectively, for Bi_2O_3 and Co_3O_4 as shown in Table 2. In contrast, the rate constant increased to 1.25×10^{-1} min^{-1} for Bi_2O_3/Co_3O_4. This result reveals that Bi_2O_3/Co_3O_4 has much higher photoreactivity than Bi_2O_3 and Co_3O_4 powder, respectively, and the rate constants increase about 5.3 and 43.1 times compared with Bi_2O_3 and Co_3O_4, respectively.

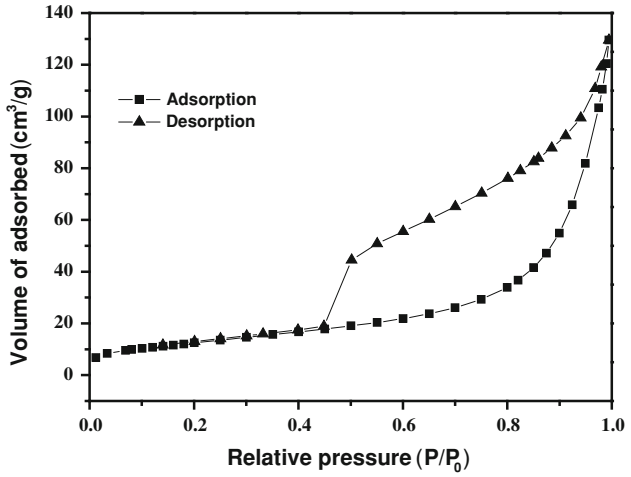

Fig. 5 Nitrogen adsorption–desorption isotherm of as-synthesized porous Bi_2O_3/Co_3O_4 catalyst

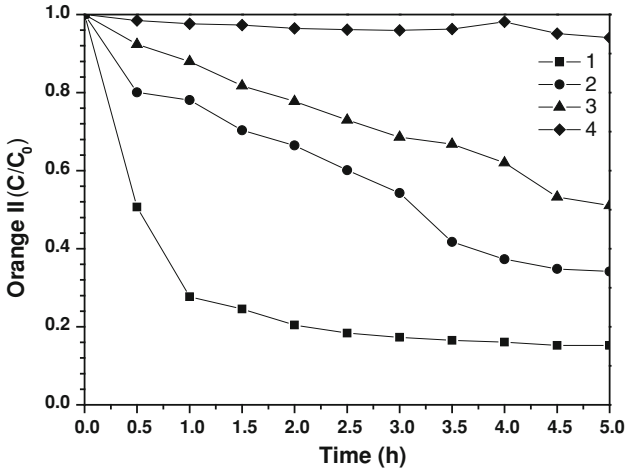

Fig. 6 Photocatalytic degradation of orange II by visible light illumination (*1*) in the presence of Bi_2O_3/Co_3O_4, (*2*) in the presence of Bi_2O_3, (*3*) in the presence of Co_3O_4, and (*4*) in the absence of any photocatalyst

Table 2 Rate constants of photocatalytic degradation by Bi_2O_3/Co_3O_4, Bi_2O_3 and Co_3O_4

	Bi_2O_3/Co_3O_4	Bi_2O_3	Co_3O_4
Rate constants (min^{-1})	1.25×10^{-1}	2.34×10^{-2}	2.9×10^{-3}

Therefore, we can conclude that optical properties and surface areas should play an important role in the photocatalytic degradation of Orange II solution since cobalt oxide is composed with many nanoparticles and the porous hollow structure of Bi_2O_3/Co_3O_4 composite microsphere. Yu et al. [22] reported the hierarchical macro-/mesoporous structures are beneficial to enhance the adsorption efficiency of light. The higher surface area and porous structure, the more reactants (e.g., O_2, OH^-, and pollutant molecules) which should be adsorbed on its surface and thus leading to superior photocatalytic activity [23]. In addition to the photocatalysis mechanisms by electron migration from valence band to conduction band under visible light illumination, the dye molecules adsorbed on the photocatalyst can also absorb visible light to produce the excited state OII_{ads}*. The oxidation potential of the excited state is more negative than the potential of the conduction band of Bi_2O_3/Co_3O_4 particles and an electron is then injected into the conduction band of Bi_2O_3/Co_3O_4 from the excited state OII_{ads}* [24]. Therefore, the electrons in the conduction band of Bi_2O_3/Co_3O_4 can react with absorbed oxygen to produce a superoxide anion radical ($^{\bullet}O_2^-$), which can further decompose the dye. At the same time, the highly oxidative holes in valence band (VB) not only directly degrade the dye molecules adsorbed on the surface of Bi_2O_3/Co_3O_4, but also are trapped by OH^- to produce hydroxyl radical species ($^{\bullet}OH$) as Eq. (1)–(4):

$$\begin{aligned} &Bi_2O_3/Co_3O_4 + h\nu(>400nm) \rightarrow Bi_2O_3/Co_3O_4(e_{CB}^- + h_{VB}^+) \\ &OII_{ads} + h\nu(>400nm) \rightarrow OII_{ads}^* \end{aligned} \quad (1)$$

$$OII_{ads}^* + Bi_2O_3/Co_3O_4 \rightarrow OII_{ads}^+ + Bi_2O_3/Co_3O_4(e^-) \quad (2)$$

$$O_2 + e^- \rightarrow^{\bullet} O_2^- \quad (3)$$

$$h^+ + OH^- \rightarrow^{\bullet} OH \quad (4)$$

These radicals, which serve as a strong oxidant, would react with the surrounding organic dye molecules and lead to the degradation by-products or mineralization into CO_2, H_2O, and mineral acids.

4 Conclusions

New visible-light-responsive Bi_2O_3/Co_3O_4 microspheres, which are assembled from nanosheets with porous structure, have been successfully synthesized by hydrothermal method in ethylene glycol (EG) with the addition of PEG and sodium acetate. NaAc can increase alkalinity of reaction system after hydrolysis, which favors the reduction of $Co(NO_3)_3$ to Co_3O_4. PEG can enter into the initial product because of the similar structure and composition with EG which plays an important role in the formation process of porous microspheres. According to the photocatalysis results, it could be concluded that the formation of Bi_2O_3/Co_3O_4 composite photocatalyst is more effective than pristine Bi_2O_3 and Co_3O_4 photocatalyst, respectively, by acquiring better visible light activities.

Acknowledgments The authors acknowledge the financial support from the National Science Council (NSC) in Taiwan under the contract number of 100-2632-E-035-001-MY3.

References

1. Pan JH, Dou H, Xiong Z, Xu C, Ma J, Zhao XS (2010) J Mater Chem 20:4512
2. Maeda K, Domen K (2007) J Phys Chem C 111:7851
3. Liu Z, Bai H, Sun D (2011) Appl Catal B 104:234
4. Muruganandham M, Amutha R, Lee GJ, Hsieh SH, Wu JJ, Sillanpaa M (2012) J Phys Chem C 116:12906
5. Anandan S, Wu JJ (2009) Mater Lett 63:2387
6. Anandan S, Lee GJ, Chen PK, Fan CH, Wu JJ (2010) Ind Eng Chem Res 49:9729
7. Hsieh SH, Lee GJ, Chen CY, Chen JH, Ma SH, Horng TL, Wu JJ (2012) J Nanosci Nanotechnol 12:5930
8. Duan F, Zheng Y, Liu L, Chen M, Xie Y (2010) Mater Lett 64:1566
9. Tseng TK, Choi J, Jung DW, Davidson M, Holloway PH (2010) ACS Appl Mater Interfaces 2:943
10. Li L, Yan B (2009) J Noncryst Solids 355:776
11. Cao AM, Hu JS, Liang HP, Song WG, Wan LJ, He XL, Gao XG, Xia SH (2006) J Phys Chem C 110:15858
12. Yang YP, Huang KL, Liu RS, Wang LP, Zeng WW, Zhang PM (2007) Trans Nonferrous Met Soc China 17:1082
13. Daneshvar N, Rasoulifard MH, Khataee AR, Hosseinzadeh F (2007) J Hazard Mater 143:95
14. Zhang FX, Saxena SK (2006) Appl Phys Lett 88:141926
15. Goldoni A, del Pennino U, Parmigiani F, Sangaletti L, Revcolevschi A (1994) Phys Rev B 50:10435
16. Zhang Y, Li YD (2004) J Phys Chem B 108:7805
17. Tao F, Gao C, Wen Z, Wang Q, Li J, Xu Z (2009) J Solid State Chem 182:1055
18. Chen Y, Hu L, Wang M, Min Y, Zhang Y (2009) Colloid Surf A 336:64
19. Luo B, Song XJ, Zhang F, Xia A, Yang WL, Hu JH, Wang CC (2010) Langmuir 26:1674
20. Petitto SC, Langell MA (2004) J Vac Sci Technol A 22:1690
21. Xiong S, Yuan C, Zhang X, Xi B, Qian Y (2009) Chem Eur J 15:5320
22. Yu J, Zhang L, Cheng B, Su Y (2007) J Phys Chem C 111:10582
23. Zheng YH, Chen CG, Zhan YY, Lin XY, Zheng Q, Wei KM, Zhu JF, Zhu YI (2007) Inorg Chem 46:6675
24. Helaili N, Bessekhouad Y, Bouguelia A, Trari M (2010) Sol Energy 84:1187